ARTICLES
PUBLISHED ONLINE: 5 DECEMBER 2016 | DOI: 10.1038/NMAT4810

nature materials

Oxygen vacancies enhance pseudocapacitive charge storage properties of MoO_{3-x}

Hyung-Seok Kim[1], John B. Cook[2,3], Hao Lin[1], Jesse S. Ko[1], Sarah H. Tolbert[1,2,3]*, Vidvuds Ozolins[1]* and Bruce Dunn[1,3]*

The short charging times and high power capabilities associated with capacitive energy storage make this approach an attractive alternative to batteries. One limitation of electrochemical capacitors is their low energy density and for this reason, there is widespread interest in pseudocapacitive materials that use Faradaic reactions to store charge. One candidate pseudocapacitive material is orthorhombic MoO_3 (α-MoO_3), a layered compound with a high theoretical capacity for lithium (279 mA h g^{-1} or 1,005 C g^{-1}). Here, we report on the properties of reduced α-MoO_{3-x}(R-MoO_{3-x}) and compare it with fully oxidized α-MoO_3 (F-MoO_3). The introduction of oxygen vacancies leads to a larger interlayer spacing that promotes faster charge storage kinetics and enables the α-MoO_3 structure to be retained during the insertion and removal of Li ions. The higher specific capacity of the R-MoO_{3-x} is attributed to the reversible formation of a significant amount of Mo^{4+} following lithiation. This study underscores the potential importance of incorporating oxygen vacancies into transition metal oxides as a strategy for increasing the charge storage kinetics of redox-active materials.

Electrochemical energy storage continues to be an exceedingly active field for research and development because of application areas ranging from portable electronics to electrification of transportation to coupling with renewable energy sources for powering the electrical grid[1]. Both batteries and electrochemical capacitors involve electrochemical mechanisms, albeit different ones, which determine their respective energy storage and power characteristics[2]. Electrical double-layer capacitors (EDLCs), also known as supercapacitors, offer higher power, shorter charging times and longer cycle life than lithium-ion batteries. The low energy density of carbon-based EDLCs, however, limits this technology. To improve on energy density, researchers have begun to investigate another mechanism for capacitive energy storage known as pseudocapacitance, where charge storage occurs via Faradaic charge transfer at or near the surface of the material[3]. The alluring feature of pseudocapacitance is the prospect of increasing energy density without compromising the high power or cycle life of carbon-based EDLCs. A number of transition metal oxides, both in aqueous and non-aqueous electrolytes, have been shown to exhibit pseudocapacitance or at least to exhibit electrochemical signatures that are representative of pseudocapacitance[4–8].

The present paper elucidates and discusses the electrochemical properties of oxygen-deficient MoO_3, which retains the layered orthorhombic structure of the parent material, α-MoO_3 (Fig. 1a–c). The electrochemical properties of α-MoO_3 have been investigated by several research groups because it is an attractive electrode material for lithium intercalation due to its high theoretical capacity (1,005 C g^{-1})[9–14]. However, low electrical conductivity and modest reaction kinetics prevent the widespread use of α-MoO_3. Moreover, during the first lithiation cycle, α-MoO_3 undergoes an irreversible phase transition around 2.8 V (versus Li/Li^+) leading to limited cycling lifetimes[10,15]. Although the preparation of various nanostructured morphologies is known to increase the lithium-ion capacity, this capacity decreases with cycling, probably due to the phase transitions mentioned above that continue to plague this material[12,16–20].

To overcome these problems, several approaches have been explored[21,22]. Pre-lithiation of α-MoO_3 increases the van der Waals (vdW) gap, thereby leading to better electrochemical cycling, although this behaviour comes at the expense of specific capacity because of the reduced oxidation state[21]. Ammonolysed α-MoO_3 showed higher electrical conductivity than α-MoO_3, but the capacity decreased significantly at increased charging rates[22]. These studies suggest that while widening the vdW gap and increasing the intrinsic electrical conductivity of α-MoO_3 may provide partial solutions to the limitations of this material, accomplishing this by adding cations to the system comes at the cost of both energy density and power density.

Although lithium intercalation in α-MoO_3 has been the subject of several studies, only a few have focused on its pseudocapacitive properties. An interesting feature reported with aqueous electrolyte is that multiple valence states are observed, namely Mo^{6+}, Mo^{5+} and Mo^{4+}, which occur as a function of potential[23]. With non-aqueous Li-ion electrolytes, it was established that a significant level of pseudocapacitive charge storage was obtained for composite electrodes consisting of α-MoO_3 nanobelts and carbon nanotubes; however, the material exhibited poor cycling behaviour due to the irreversible structural changes occurring during the first cycle[14]. Pseudocapacitive contributions to charge storage were also reported for mesoporous crystalline α-MoO_3 films[24]. The corresponding mesoporous amorphous MoO_3 films exhibited significantly lower levels of capacitive charge storage, suggesting that near-surface intercalation was contributing to pseudocapacitance in the crystalline, but not the amorphous materials.

Another viable route for overcoming the low electrical conductivity of α-MoO_3 is through the introduction of oxygen vacancies[25,26]. This approach has been shown to improve the

[1]Department of Materials Science and Engineering, UCLA, Los Angeles, California 90095-1595, USA. [2]Department of Chemistry and Biochemistry, UCLA, Los Angeles, California 90095-1569, USA. [3]The California NanoSystems Institute, UCLA, Los Angeles, California 90095, USA.
*e-mail: tolbert@chem.ucla.edu; vidvuds@ucla.edu; bdunn@ucla.edu

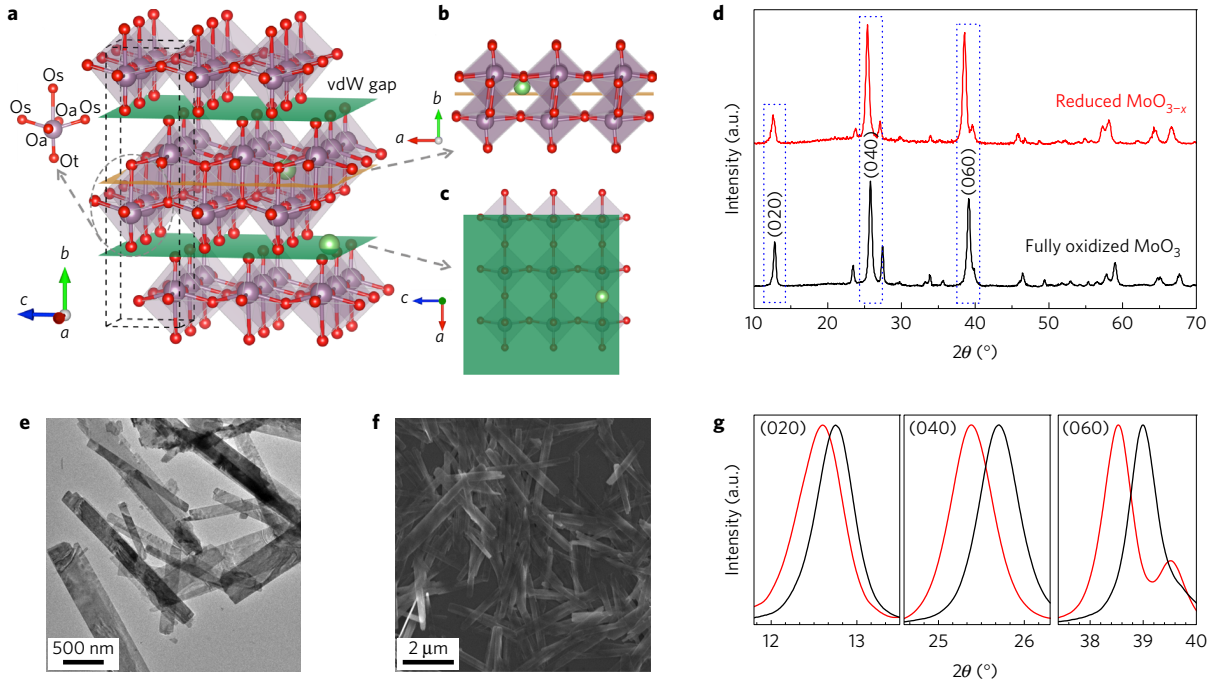

Figure 1 | Structural analysis of as-prepared α-MoO_3. a, Crystal structure of α-MoO_3. The structural framework consists of a bilayer network of edge-sharing MoO_6 octahedra (shown in grey). The bilayers are stacked along the *b* direction and bonded to adjacent layers by van der Waals forces. There are three types of oxygen anion. The 'terminal oxygen' (O_t) results in a Mo–O_t bond that points perpendicular to the vdW gap (shown in green). The second type, labelled as O_a, forms asymmetric bonds with two Mo ions in the *a* direction, while the third type, referred to as 'symmetric oxygen' (O_s), has three-fold symmetry that leads to the formation of two short bonds with two Mo ions in the [001] direction and one longer bond with a Mo ion in the [010] direction. **b**,**c**, Possible lithium intercalation sites at intralayer (**b**) and at interlayer (**c**) of the α-MoO_3. The 'interlayer site' is located between two octahedral bilayers while the 'intralayer site' is in the one-dimensional tunnel ([001] direction) within the bilayer sheets. **d**, XRD patterns for R-MoO_{3-x} (red), and F-MoO_3 (black). The strong diffraction intensity for the (020), (040) and (060) peaks indicates that the as-synthesized α-MoO_3 powders preferentially orient along the [0*k*0] direction. **e**, TEM image of R-MoO_{3-x}. **f**, SEM image of R-MoO_{3-x}. **g**, Selected XRD pattern insets of the (020), (040) and (060) diffraction peaks that compare R-MoO_{3-x} (red), and F-MoO_3 (black). The peak position shifts to a lower angle indicating expansion of the vdW gap in oxygen-deficient α-MoO_3.

electrical conductivity of some transition metal oxides because oxygen vacancies can act as shallow donors and thereby increase the carrier concentration[27,28]. There have been only a few studies that explore the effect of oxygen non-stoichiometry and enhanced electrical conduction on energy storage properties[29,30]. These limited results suggest that the presence of oxygen vacancies produces greater electrical conductivity and, in the case of α-MoO_3, an expanded interlayer distance[27]. Both of these features are likely to lead to improved electrochemical performance. In the present paper, we have carried out a comprehensive study that examines the effects of oxygen vacancies on the structure, chemistry, and charge storage properties of α-MoO_3. The introduction of vacancies leads to faster kinetics and preserves the α-MoO_3 structure, which enables extended cycling with lithium to occur with minimal decrease in charge storage. Density-functional theory (DFT) calculations provide insight regarding vacancy sites, electronic properties and lithium intercalation voltages for R-MoO_{3-x}.

Material synthesis, characterization and DFT calculations

R-MoO_{3-x} was prepared by microwave-activated hydrothermal synthesis[31–33]. The X-ray diffraction (XRD) pattern for the as-synthesized material (red) is shown in Fig. 1d. The major reflections can be indexed with a *Pbnm* space group corresponding to α-MoO_3, in good agreement with JCPDS No. 35-0609. Since α-MoO_3 is white powder, it is surprising that the colour of the as-synthesized material was deep blue (see inset of Supplementary Fig. 1a). This indicates that as-synthesized MoO_3 was reduced during the synthesis treatment. The shape and size of R-MoO_{3-x} were characterized by transmission electron microscopy (TEM; Fig. 1e) and scanning electron microscopy (SEM) (Fig. 1f). The materials are in the form of nanobelts that are 100 to 500 nm in width and 3 ~ 5 μm in length. The thickness of individual R-MoO_{3-x} nanobelts was determined by atomic force microscopy to be about 10 nm (Supplementary Fig. 2).

The oxygen vacancy concentration of R-MoO_{3-x} was characterized using thermogravimetric analysis (TGA). TGA of R-MoO_{3-x} (Supplementary Fig. 3) indicates that the reduced material reacts with oxygen on heating, leading to a lower mass loss compared with the TGA in argon. From the calculations, we estimate that the composition of the R-MoO_{3-x} corresponds to $MoO_{2.87}$. To complement these calculations, X-ray photoelectron spectroscopy (XPS) was used to characterize the oxidation state of molybdenum (Fig. 2a,b). The R-MoO_{3-x} has a significant amount of Mo^{5+}, much of which is still observed even after appreciable argon plasma etching to remove the outer surface layer. The calculated stoichiometries based on molybdenum and oxygen XPS peak areas are $MoO_{2.91}$ and $MoO_{2.83}$ for surface and bulk (that is, after etching), respectively. These values are comparable to those determined from TGA. These results establish that the oxygen vacancies are not limited to the surface, and that they extend throughout the bulk of the material.

We used DFT calculations to provide greater insight into the oxygen vacancy sites and polaron configurations that are present in R-MoO_{3-x}. The formation enthalpies for an oxygen vacancy in various oxygen sites and for different polaron configurations are listed in Table 1. We find that the oxygen vacancy configuration with the lowest formation enthalpy (1.32 eV) corresponds to an

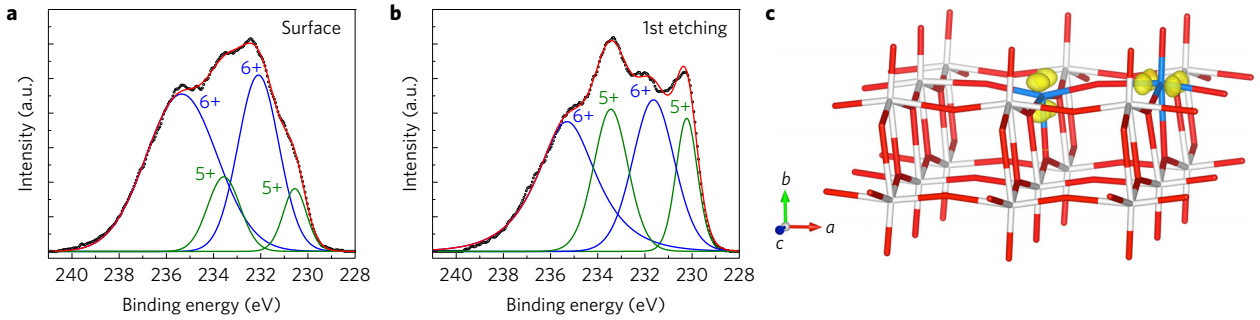

Figure 2 | Characterization of oxygen vacancies in α-MoO_3. a,b, High-resolution XPS spectra of as-synthesized R-MoO_{3-x} in the Mo 3*d* region (before (**a**) and after (**b**) argon plasma etching). **c**, The most stable oxygen vacancy configuration and polaron formation in R-MoO_{3-x} calculated from DFT. The Mo^{5+} ions are highlighted with blue.

oxygen vacancy at the O_t site and two Mo^{5+} ions (bipolaron) near the defect centre (see Fig. 2c). In this configuration, one polaron occupies the d_{yz} orbital of the Mo^{5+} ion at the defect site, while the other one fills in the d_{xz} orbital of the Mo^{5+} ion next to the defect centre in the *a* direction. A vacancy structure at the O_t site, where two polarons occupy the d_{xy} and d_{yz} orbitals of the five-fold coordinated Mo^{4+} ion at the defect, is 0.19 eV higher in energy. The formation of oxygen vacancies at the O_a and O_s sites is significantly less favourable than at the O_t site. This is in agreement with our measured XPS spectra where no Mo^{4+} oxidation states are seen (see Fig. 2a,b). Detailed results for the polaron configurations, polaron binding energies and variations of structural parameters are given in the Supplementary Information.

Electrochemical behaviour

To understand the influence of oxygen vacancies on electrochemical behaviour, the R-MoO_{3-x} was subjected to heat treatments that fully oxidize the MoO_3. After heat treatment, the phase of each material was confirmed by XRD to have the α-MoO_3 structure (Fig. 1d). No significant change in nanobelt morphology was evident from TEM (Supplementary Fig. 1) and the small differences in surface areas (Supplementary Table 1) are not likely to affect the electrochemistry of α-MoO_3.

There are two distinguishable lithium intercalation sites in α-MoO_3 (Fig. 1b,c). Charge storage occurs mainly by the insertion of lithium ions into the interlayer site to form lithiated MoO_3(Li_xMoO_3, $x_{max}=1.5$)[9].

$$MoO_3 + xLi^+ + xe^- \rightarrow Li_xMoO_3 \quad (1)$$

Sweep voltammetry measurements were used to characterize the electrochemical properties. The electrodes used in these experiments contained no carbon or binder so that the electrochemical properties of the different oxides were determined directly from the measurements. Results show that R-MoO_{3-x} has higher capacity and faster kinetics compared with F-MoO_3 (Fig. 3a,b) At a sweep rate of 100 mV s^{-1} (charging time of 20 s), R-MoO_{3-x} stores ~550 C g^{-1}, while the capacity for the fully oxidized material is <400 C g^{-1}. This fast response underscores the capacitive nature of charge storage in R-MoO_{3-x}. In addition, the cycling behaviour of R-MoO_{3-x} is more stable than that of F-MoO_3 (Fig. 3c). After 50 cycles, the capacity decreased by only 5%, in contrast to the 50% decay exhibited by the F-MoO_3. Moreover, R-MoO_{3-x} exhibited very stable performance over 10,000 cycles (Supplementary Fig. 6). This behaviour suggests that by introducing oxygen vacancies, it is possible to improve the cycling stability of α-MoO_3, a feature that has been a significant limitation in the application of this material in electrochemical devices.

Sweep voltammetry also provides greater insight into the difference in charge storage kinetics. In Fig. 3d, the log(*i*) versus log(*v*) plot for the cathodic peak at ~2.4 V (versus Li/Li^+) shows that the current dependence on the sweep rate, *v*, is given by the relation[34]:

$$i = a\,v^b \quad (2)$$

A *b* value of 0.5 indicates that the current is controlled by semi-infinite diffusion while $b = 1$ indicates capacitive behaviour[35]. For R-MoO_{3-x}, the *b* value is 1, indicating the capacitor-like nature of the kinetics, which is one of the characteristic features of pseudocapacitance[36]. In contrast, F-MoO_3 exhibits values of approximately 0.7, meaning that the charge storage is affected by diffusion processes. The anodic peaks for both materials show the same general behaviour (Supplementary Fig. 7).

The increased level of pseudocapacitive charge storage for R-MoO_{3-x} is also shown using an analysis where the current response, $i(V)$, is a combination of capacitor-like and diffusion-controlled behaviours[37]:

$$i(V) = k_1 v + k_2 v^{1/2} \quad (3)$$

By determining both k_1 and k_2, it is possible to calculate, as a function of potential, the fraction of current contributed by diffusion-controlled intercalation processes and those arising from capacitor-like processes. The data shown in Fig. 3e,f indicate that capacitor-like charge storage in R-MoO_{3-x} occurs to a much greater extent compared with F-MoO_3 (75% versus 37%). In summary, the sweep voltammetry measurements show that R-MoO_{3-x} exhibits higher capacity and faster kinetics than F-MoO_3.

The voltammetric sweeps for the R-MoO_{3-x} also display two interesting differences compared with those of the F-MoO_3. The

Table 1 | Formation enthalpies of an oxygen vacancy and polaron states for bulk MoO_3.

Vacancy site	Polaron	Occupied orbitals	Formation enthalpies (eV)
O_t	Mo^{4+}	d_{xy}, d_{yz}	1.51
	Mo^{5+}, Mo^{5+}	d_{yz}, d_{xz}	1.32
O_a	Mo^{4+}	d_{xy}, d_{xz}	2.49
	Mo^{5+}, Mo^{5+}		*
O_s	Mo^{4+}		*
	Mo^{5+}, Mo^{5+}	d_{xy}, d_{xz}, d_{yz}	3.41

The asterisk superscript denotes that these structures always relax towards other configurations in the table. A vacancy at the O_a site and a Mo^{4+} ion at the defect centre are predicted to have a formation enthalpy of 2.5 eV, while the introduction of vacancy at an O_s site requires 3.4 eV. The relative ordering of the $O_t/O_a/O_s$ vacancy energies can be explained by the number of broken Mo–O bonds following removal of an O ion (one/two/three). These results indicate that the preferred site for oxygen vacancies is the O_t site and the favoured polaron configuration is on two Mo^{5+} ions near the vacancy. Furthermore, since the energy difference between two Mo^{5+} polarons and one Mo^{4+} polaron at an O_t vacancy site is 0.19 eV, we expect only a small proportion of Mo^{4+} under ambient equilibrium conditions.

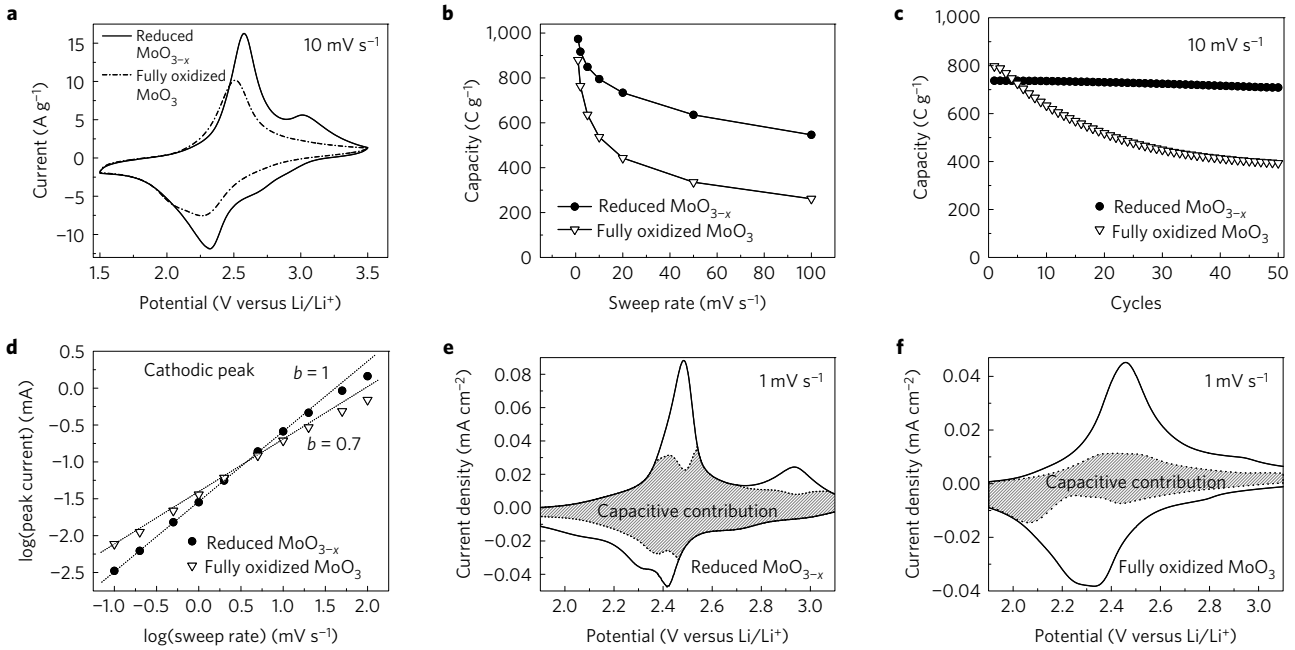

Figure 3 | Electrochemical analysis of thin-film MoO_3 electrodes. a, Voltammetric sweep at 10 mV s^{-1} for R-MoO_{3-x}, and F-MoO_3 (tenth cycle). **b**, Specific capacity as a function of sweep rate between 1 and 100 mV s^{-1}. The R-MoO_{3-x} and F-MoO_3 samples were pre-cycled at 10 mV s^{-1} for 10 cycles to stabilize their response before the measurements. **c**, Variation in specific capacity for R-MoO_{3-x} and F-MoO_3 as a function of the number of cycles at 10 mV s^{-1}. **d**, The log(i) versus log(v) plot of the cathodic current response at ~2.4 V (versus Li/Li^+). The slope of this line gives the b value, which shows that this value is close to 1 for R-MoO_{3-x} and 0.7 for F-MoO_3 for sweep rates ranging from 0.1 to 20 mV s^{-1}. **e**,**f**, k_1, k_2 analysis (equation (3)) of R-MoO_{3-x} (**e**) and F-MoO_3 (**f**) at 1 mV s^{-1} (after ten pre-cycles at 10 mV s^{-1}). These data show the contribution to capacitive charge storage as a function of potential. Capacitive charge storage for R-MoO_{3-x} is two times larger than F-MoO_3.

F-MoO_3 exhibits irreversible peaks on lithiation during its first cycle as shown in Fig. 4a. This irreversibility is attributed to the trapping of Li^+ in the intralayers of α-MoO_3, thus inducing a phase change, which results in poor electrochemical reversibility[10,15,20]. However, the R-MoO_{3-x} does not display these irreversible peaks, so that the first, second and third cycles are almost identical (Fig. 4b). The galvanostatic discharge curves are also consistent with this behaviour (see outlined boxes in insets in Fig. 4a,b). The F-MoO_3 exhibits a plateau during its first cycle, which disappears during the second cycle; R-MoO_{3-x} displays no such plateau, indicating that no structural change is occurring on cycling. Thus, R-MoO_{3-x} retains its capacity on cycling while the capacity decreases continuously for F-MoO_3 because of the structural rearrangement from the trapping of Li^+ (Fig. 3c).

A second feature in the cyclic voltammetry (CV) that is influenced by the presence of oxygen vacancies is the addition of a distinctive peak at ~3.0 V during de-intercalation (Fig. 3a,e). This peak does not occur in the F-MoO_3. To explain the existence of this additional peak, the intercalation energies for the interlayer and intralayer sites were calculated by DFT for both R-MoO_{3-x} and F-MoO_3. In F-MoO_3, the values for the interlayer and intralayer sites (see Fig. 1b,c) were 3.25 and 3.21 eV, respectively. That is, the energy difference between the two types of site is negligible. The similarity in intercalation energies for these sites leads to one main peak in the CV for F-MoO_3. The introduction of oxygen vacancies and polarons in R-MoO_{3-x}, however, breaks the symmetry of the crystal. Hence, the sites for lithium insertion no longer have the same energy. The voltages calculated for the R-MoO_{3-x} are in the range 2.96 to 3.36 V as shown in Supplementary Fig. 8. The intercalated structures with higher voltages (>3.30 V) are more likely to be observed in experiments, because these structures are thermodynamically more stable. Except for the d_{yz} polaron at the oxygen defect centre, all of the polarons stabilize in the d_{xz} orbitals of the Mo^{5+} ions. The distance between the lithium intercalation site and the oxygen vacancy centre together with the different polaron configurations contributes to the spread of the intercalation voltages.

Structure and chemical effects

The creation of oxygen vacancies in α-MoO_3 leads to a material that exhibits higher capacity, faster kinetics and better electrochemical stability compared with the fully oxidized material. In this section, we discuss the structural and chemical features that influence and determine these properties.

One significant structural effect associated with the development of oxygen vacancies is an increase in the vdW gap, a feature that should certainly lead to improved electrochemical kinetics. The XRD patterns in Fig. 1g show that the (020), (040) and (060) reflections, which correspond to the b-lattice plane interlayers, are shifted to lower angles in R-MoO_{3-x}. The b-lattice cell parameter, calculated from the (020) reflections, expands from 13.886 Å for F-MoO_3 to 14.062 Å in R-MoO_{3-x} (Supplementary Table 2). The development of a wider vdW gap arising from oxygen vacancies was reported previously[27] and apparently occurs here as well. DFT calculations (Supplementary Table 3) also indicate that the vdW gap will expand in R-MoO_{3-x} due to an oxygen vacancy at the O_t site with two accompanying Mo^{5+} ions.

A second structural consideration is the difference in the cycling-induced phase behaviour between R-MoO_{3-x} and F-MoO_3. The irreversible electrochemical changes shown in Fig. 4a for F-MoO_3 were also observed using *ex situ* XRD (Fig. 4c). Following lithiation, the XRD pattern becomes mostly featureless, with a few broad peaks that are shifted from the peak position of the parent material. While the poor crystallographic order differs from previous reports on bulk α-MoO_3, the positions of the broad peaks are in agreement with previous reports for the new phase[10,15,38]. After delithiation (3.5 V), two sharper peaks are observed in the same location, again consistent with the presence of a distinctly new phase. These peaks can be indexed to the (030) and (0100) reflections of the transformed

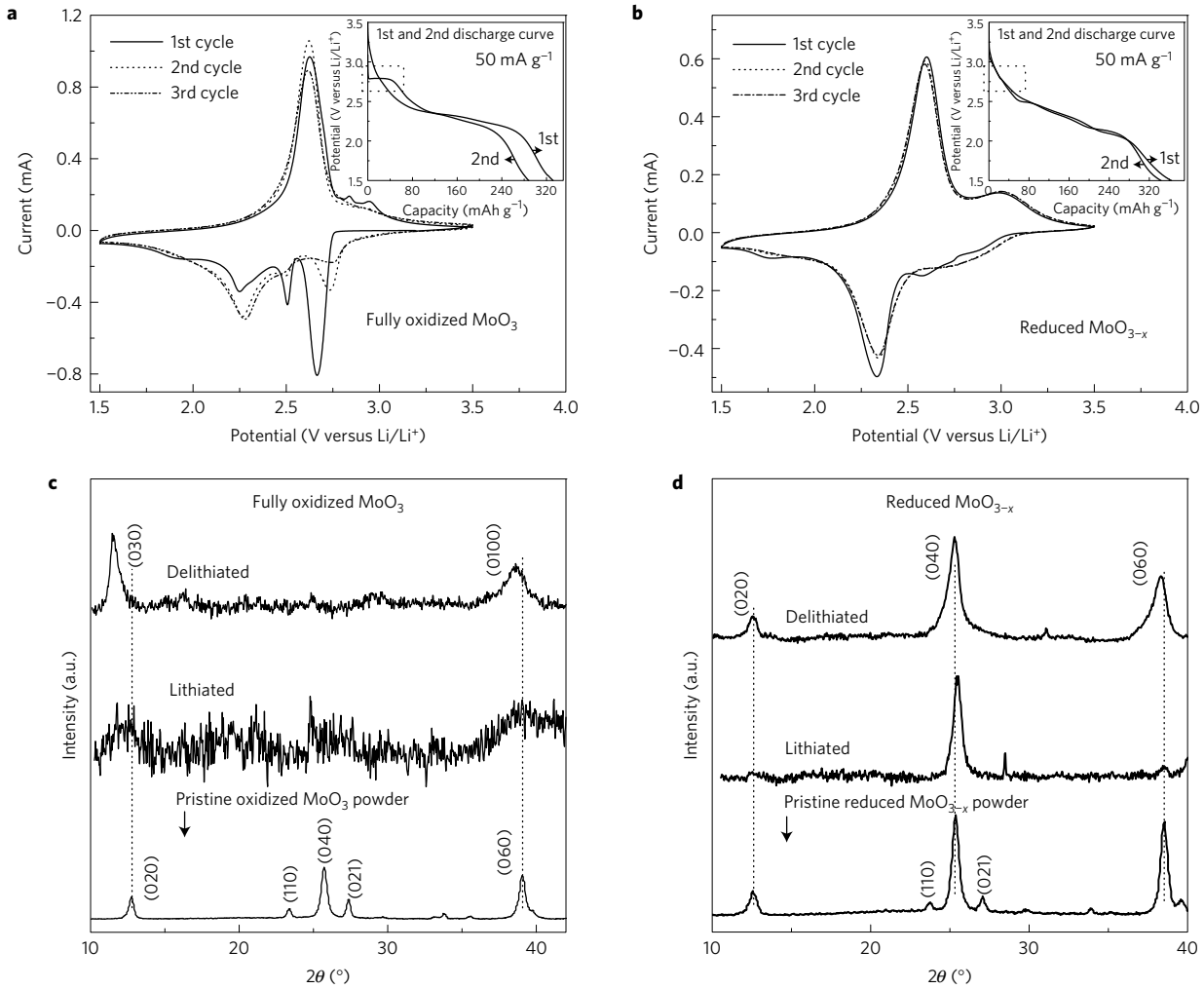

Figure 4 | Structural characterization of F-MoO_3 and R-MoO_{3-x} associated with electrochemical cycling. a,**b**, Cyclic voltammetry of the first three cycles at 10 mV s^{-1} and galvanostatic discharge curves (insets, at 50 mA g^{-1}) in F-MoO_3 (**a**), and R-MoO_{3-x} (**b**). **c**,**d**, *Ex situ* XRD at the lithiated (at 1.5 V) and delithiated (at 3.5 V) states in F-MoO_3 (**c**) and R-MoO_{3-x} (**d**). The data show that the F-MoO_3 undergoes a phase transformation driven by lithium insertion, but the phase transformation is suppressed in the R-MoO_{3-x}. (The pristine powder XRD patterns show the (110) and (021) reflections while the cycled samples do not.)

phase, and cannot be indexed as the (020) and (060) reflections of the parent structure. Therefore, we conclude that lithium insertion drives an irreversible electrochemically induced phase transition in the F-MoO_3.

In contrast, R-MoO_{3-x} does not undergo a phase transformation following lithiation to 1.5 V (Fig. 4d). The (0*k*0) diffraction peaks for R-MoO_{3-x} are slightly shifted to higher 2θ (smaller *d*-spacing) in the lithiated material, which might be due to Coulombic interactions in the intercalated state. In both the pristine material and the lithiated phase, XRD peaks can be indexed to the (020) reflection and the higher-order overtones, (040) and (060), indicating that the material has not undergone a phase transition. This behaviour is in sharp contrast to the phase transition observed in F-MoO_3. After full delithiation, the diffraction can still be indexed to the (020), (040) and (060) diffraction peaks of the parent structure, though with a slightly expanded lattice constant. These structural data thus give clear evidence that the electrochemically induced phase transition is suppressed in R-MoO_{3-x}. This conclusion is corroborated by the fact that we do not see an irreversible peak at 2.7 V in the CV of R-MoO_{3-x}. The expanded lattice galleries in R-MoO_{3-x} are apparently large enough that a phase transition is no longer energetically needed to accommodate lithium into the structure. We have previously shown that minimizing structural change following lithium intercalation, and suppression of phase transitions are hallmarks of pseudocapacitance[39–41]. As a result, the differences in phase stability between the R-MoO_{3-x} and the F-MoO_3 explain why R-MoO_{3-x} exhibits more stable cycling performance and faster kinetics compared with F-MoO_3.

One interesting question concerning the electrochemical properties of R-MoO_{3-x} is that its capacity is higher than F-MoO_3, despite the fact that the R-MoO_{3-x} has a lower average oxidation state. As discussed above, the improved rate capability and electrochemical stability of the R-MoO_{3-x} can be well explained by structural modifications that result from the formation of oxygen vacancies. It is not at all clear, however, how these oxygen vacancies could also lead to the higher capacity observed in the reduced material (Fig. 3b). To examine this issue, *ex situ* XPS (Fig. 5) was performed on both F-MoO_3 and R-MoO_{3-x} at the same potentials, that is, after full lithiation at 1.5 V and after delithiation at 3.5 V (both versus Li/Li^+). The most interesting feature in the XPS spectra is the presence of Mo^{4+} following lithiation for both R-MoO_{3-x} and F-MoO_3. For the R-MoO_{3-x}, the fraction of Mo^{4+} is ~40% (Fig. 5c). Despite this significant amount of Mo^{4+}, the α-MoO_3 structure was retained and XRD showed no evidence of MoO_2 (Fig. 4d). By comparison, the F-MoO_3 contains only ~20% Mo^{4+} (Fig. 5d). Another interesting characteristic is the ratio of

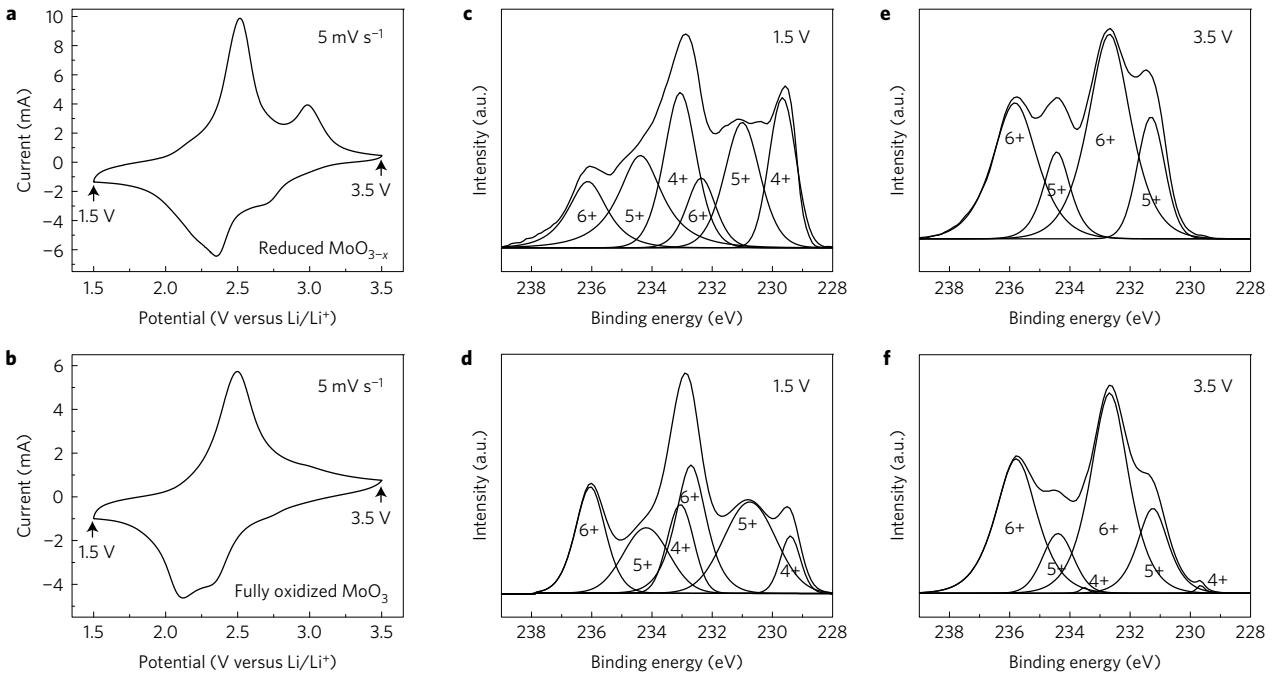

Figure 5 | Effect of oxygen vacancies on the presence of Mo^{4+} and Mo^{5+} oxidation states during electrochemical cycling. a,b, Voltammetric sweeps at 5 mV s^{-1} for R-MoO_{3-x} (**a**) and F-MoO_3 (**b**). The samples were pre-cycled at 10 mV s^{-1} for five cycles before the measurements. **c–f**, High-resolution XPS spectra of the Mo 3*d* region in R-MoO_{3-x} at the lithiated (**c**) and delithiated state (**e**), and in F-MoO_3 at the lithiated state (**d**) and delithiated state (**f**).

Mo^{4+}/Mo^{6+} in each of the materials. For the R-MoO_{3-x}, this ratio is ∼2 whereas for the F-MoO_3, the ratio is ∼0.8. These results thus indicate that the difference in capacity between R-MoO_{3-x} and F-MoO_3 arises from increased conversion of Mo^{6+} to Mo^{4+}, rather than Mo^{5+}, following lithiation. If the Mo^{5+}-based polarons in R-MoO_{3-x} lead to increased stability of Mo^{4+} sites, then this provides a viable mechanism for achieving higher capacity in the reduced material.

The *ex situ* XPS spectra also provide insight concerning the electrochemical reversibility of the two materials. When delithiated at 3.5 V, the R-MoO_{3-x} contains only Mo^{6+} and Mo^{5+}, whereas the F-MoO_3 possesses both of these ions along with a small amount of residual Mo^{4+} (Fig. 5e,f). The latter indicates that some Li^+ remains trapped in the MoO_3 structure, probably due to the structural phase transition discussed above (Fig. 4c).

In this work we have demonstrated that the introduction of oxygen vacancies into the α-MoO_3 lattice leads to improved electrochemical properties. The incorporation of oxygen vacancies leads to a larger interlayer spacing along the *b* axis that promotes faster kinetics and enables the α-MoO_3 structure to be retained during the insertion and removal of Li ions. The absence of any phase transition following lithiation results in significantly improved cycle life for R-MoO_{3-x}, in agreement with previous results on pseudocapacitive materials. The high specific capacity in R-MoO_{3-x} can be explained by increased Mo^{4+} formation following lithiation, a process that occurs reversibly and without the development of the monoclinic MoO_2 in R-MoO_{3-x}. This work thus demonstrates that the energy storage properties of α-MoO_3 are improved substantially by the introduction of oxygen vacancies. We believe that the incorporation of oxygen vacancies into other transition metal oxides could lead to a wide range of materials whose properties are extremely attractive for pseudocapacitive charge storage.

Methods

Methods and any associated references are available in the online version of the paper.

Received 19 January 2016; accepted 28 October 2016; published online 5 December 2016

References

1. Stevenson, K. J., Ozolins, V. & Dunn, B. Electrochemical energy storage. *Acc. Chem. Res.* **46,** 1051–1052 (2013).
2. Miller, J. R. & Simon, P. Electrochemical capacitors for energy management. *Science* **321,** 651–652 (2008).
3. Simon, P., Gogotsi, Y. & Dunn, B. Where do batteries end and supercapacitors begin? *Science* **343,** 1210–1211 (2014).
4. Lee, H. Y. & Goodenough, J. B. Ideal supercapacitor behavior of amorphous $V_2O_5nH_2O$ in potassium chloride (KCl) aqueous solution. *J. Solid State Chem.* **148,** 81–84 (1999).
5. Toupin, M., Brousse, T. & Bélanger, D. Charge storage mechanism of MnO_2 electrode used in aqueous electrochemical capacitor. *Chem. Mater.* **16,** 3184–3190 (2004).
6. Zheng, J. P., Cygan, P. J. & Jow, T. R. Hydrous ruthenium oxide as an electrode material for electrochemical capacitors. *J. Electrochem. Soc.* **142,** 2699–2703 (1995).
7. Brousse, T. *et al*. Long-term cycling behavior of asymmetric activated carbon/MnO_2 aqueous electrochemical supercapacitor. *J. Power Sources* **173,** 633–641 (2007).
8. Brezesinski, K. *et al*. Pseudocapacitive contributions to charge storage in highly ordered mesoporous group V transition metal oxides with iso-oriented layered nanocrystalline domains. *J. Am. Chem. Soc.* **132,** 6982–6990 (2010).
9. Li, W., Cheng, F., Tao, Z. & Chen, J. Vapor-transportation preparation and reversible lithium intercalation/deintercalation of α-MoO_3 microrods. *J. Phys. Chem. B* **110,** 119–124 (2006).
10. Tsumura, T. & Inagaki, M. Lithium insertion/extraction reaction on crystalline MoO_3. *Solid State Ion.* **104,** 183–189 (1997).
11. Zhou, L. *et al*. α-MoO_3 nanobelts: a high performance cathode material for lithium ion batteries. *J. Phys. Chem. C* **114,** 21868–21872 (2010).
12. Lee, S. H. *et al*. Reversible lithium-ion insertion in molybdenum oxide nanoparticles. *Adv. Mater.* **20,** 3627–3632 (2008).
13. Chernova, N. A., Roppolo, M., Dillon, A. C. & Whittingham, M. S. Layered vanadium and molybdenum oxides: batteries and electrochromics. *J. Mater. Chem.* **19,** 2526–2552 (2009).
14. Mendoza-Sánchez, B. & Grant, P. S. Charge storage properties of a α-MoO_3/carboxyl-functionalized single-walled carbon nanotube composite electrode in a Li ion electrolyte. *Electrochim. Acta* **98,** 294–302 (2013).
15. Iriyama, Y., Abe, T., Inaba, M. & Ogumi, Z. Transmission electron microscopy (TEM) analysis of two-phase reaction in electrochemical lithium insertion within α-MoO_3. *Solid State Ion.* **135,** 95–100 (2000).

16. Chen, J. S., Cheah, Y. L., Madhavi, S. & Lou, X. W. Fast synthesis of α-MoO_3 nanorods with controlled aspect ratios and their enhanced lithium storage capabilities. *J. Phys. Chem. C* **114,** 8675–8678 (2010).
17. Reddy, C. V. S., Walker, E. H., Wen, C. & Mho, S. I. Hydrothermal synthesis of MoO_3 nanobelts utilizing poly(ethylene glycol). *J. Power Sources* **183,** 330–333 (2008).
18. Hassan, M. F., Guo, Z. P., Chen, Z. & Liu, H. K. Carbon-coated MoO_3 nanobelts as anode materials for lithium-ion batteries. *J. Power Sources* **195,** 2372–2376 (2010).
19. Riley, L. A., Lee, S. H., Gedvilias, L. & Dillon, A. C. Optimization of MoO_3 nanoparticles as negative-electrode material in high-energy lithium ion batteries. *J. Power Sources* **195,** 588–592 (2010).
20. Kang, J. H., Paek, S. M. & Choy, J. H. *In situ* X-ray absorption spectroscopic study for α-MoO_3 electrode upon discharge/charge reaction in lithium secondary batteries. *Bull. Korean Chem. Soc.* **31,** 3675–3678 (2010).
21. Mai, L. *et al*. Lithiated MoO_3 nanobelts with greatly improved performance for lithium batteries. *Adv. Mater.* **19,** 3712–3716 (2007).
22. Wang, X.-J., Nesper, R., Villevieille, C. & Novák, P. Ammonolyzed MoO_3 nanobelts as novel cathode material of rechargeable Li-ion batteries. *Adv. Energy Mater.* **3,** 606–614 (2013).
23. Mendoza-Sánchez, B. *et al*. An investigation of nanostructured thin film α-MoO_3 based supercapacitor electrodes in an aqueous electrolyte. *Electrochim. Acta* **91,** 253–260 (2013).
24. Brezesinski, T., Wang, J., Tolbert, S. H. & Dunn, B. Ordered mesoporous α-MoO_3 with iso-oriented nanocrystalline walls for thin-film pseudocapacitors. *Nat. Mater.* **9,** 146–151 (2010).
25. Balendhran, S. *et al*. Enhanced charge carrier mobility in two-dimensional high dielectric molybdenum oxide. *Adv. Mater.* **25,** 109–114 (2013).
26. Hu, X. K. *et al*. Comparative study on MoO_3 and H_xMoO_3 nanobelts: structure and electric transport. *Chem. Mater.* **20,** 1527–1533 (2008).
27. Dieterle, M., Weinberg, G. & Mestl, G. Raman spectroscopy of molybdenum oxides: part I. Structural characterization of oxygen defects in MoO_{3-x} by DR UV/VIS, Raman spectroscopy and X-ray diffraction. *Phys. Chem. Chem. Phys.* **4,** 812–821 (2002).
28. Wang, G., Ling, Y. & Li, Y. Oxygen-deficient metal oxide nanostructures for photoelectrochemical water oxidation and other applications. *Nanoscale* **4,** 6682–6691 (2012).
29. Lu, X. *et al*. Hydrogenated TiO_2 nanotube arrays for supercapacitors. *Nano Lett.* **12,** 1690–1696 (2012).
30. Shin, J.-Y., Joo, J. H., Samuelis, D. & Maier, J. Oxygen-deficient $TiO_{2-\delta}$ nanoparticles via hydrogen reduction for high rate capability lithium batteries. *Chem. Mater.* **24,** 543–551 (2012).
31. Xu, L. *et al*. 3D flowerlike α-nickel hydroxide with enhanced electrochemical activity synthesized by microwave-assisted hydrothermal method. *Chem. Mater.* **20,** 308–316 (2008).
32. Murugan, A. V., Muraliganth, T. & Manthiram, A. Comparison of microwave assisted solvothermal and hydrothermal syntheses of $LiFePO_4$/C nanocomposite cathodes for lithium ion batteries. *J. Phys. Chem. C* **112,** 14665–14671 (2008).
33. Cook, J. B., Kim, C., Xu, L. & Cabana, J. The effect of Al substitution on the chemical and electrochemical phase stability of orthorhombic $LiMnO_2$. *J. Electrochem. Soc.* **160,** A46–A52 (2013).
34. Lindström, H. *et al*. Li^+ ion insertion in TiO_2 (anatase). 2. Voltammetry on nanoporous films. *J. Phys. Chem. B* **101,** 7717–7722 (1997).
35. Wang, J., Polleux, J., Lim, J. & Dunn, B. Pseudocapacitive contributions to electrochemical energy storage in TiO_2 (anatase) nanoparticles. *J. Phys. Chem. C* **111,** 14925–14931 (2007).
36. Augustyn, V., Simon, P. & Dunn, B. Pseudocapacitive oxide materials for high-rate electrochemical energy storage. *Energy Environ. Sci.* **7,** 1597–1614 (2014).
37. Bard, A. J. & Faulkner, L. R. *Electrochemical Methods: Fundamentals and Applications* 2nd edn (Wiley, 2001).
38. Hashem, A. M. *et al*. Two-phase reaction mechanism during chemical lithium insertion into α-MoO_3. *Ionics* **13,** 3–8 (2007).
39. Kim, H.-S., Cook, J. B., Tolbert, S. H. & Dunn, B. The development of pseudocapacitive properties in nanosized-MoO_2. *J. Electrochem. Soc.* **162,** A5083–A5090 (2015).
40. Augustyn, V. *et al*. High-rate electrochemical energy storage through Li^+ intercalation pseudocapacitance. *Nat. Mater.* **12,** 518–522 (2013).
41. Muller, G. A. *et al*. High performance pseudocapacitor based on 2D layered metal chalcogenide nanocrystals. *Nano Lett.* **15,** 1911–1917 (2015).

Acknowledgements

This work was supported as part of the Center for Molecularly Engineered Energy Materials, an Energy Frontier Research Center funded by the US Department of Energy, Office of Science, Office of Basic Energy Sciences, under award DE-SC001342 and through individual DOE grant DE-SC0014213 (S.H.T.). The XPS instrument used in this work was obtained with support from the NSF, award number 0840531. This research used resources of the National Energy Research Scientific Computing Center, a DOE Office of Science User Facility supported by the Office of Science of the US Department of Energy under Contract No. DE-AC02-05CH11231. H.L. and V.O. acknowledge financial support from the U.S. DOE under grant DE-FG02-07ER46433. Additional support was provided by the Office of Naval Research. We thank E. D. Gaspera for his experimental insights.

Author contributions

H.-S.K., J.S.K. and J.B.C.: experimental work and data analysis. H.L.: computational study. S.H.T., V.O. and B.D.: project planning and data analysis.

Additional information

Supplementary information is available in the online version of the paper. Reprints and permissions information is available online at www.nature.com/reprints. Correspondence and requests for materials should be addressed to S.H.T., V.O. or B.D.

Competing financial interests

The authors declare no competing financial interests.

Methods

Synthesis of R-MoO_{3-x}. R-MoO_{3-x} was synthesized by a one-step microwave hydrothermal synthesis. Anhydrous $MoCl_5$ (270 mg, Strem Chemicals) was dissolved in ethanol (5 ml) and deionized water (15 ml) and nitric acid (0.25 ml, Sigma-Aldrich) was added in this solution with stirring. The prepared solution was transferred into the 25 ml microwave reaction vessel and placed in a microwave synthesis system (Discover SP, CEM Corporation). The sample was heated with 200 W to 180 °C for 15 min. During the synthesis, the pressure was maintained at around 180 psi. The resulting deep-blue-coloured solution was centrifuged (5,000 r.p.m., 4,500*g*, for 5 min) and washed three times with deionized water and ethanol and dried in vacuum for 24 h. The fully oxidized samples were prepared by annealing the as-prepared samples at 400 °C for 1 h.

TGA and XPS for the oxygen vacancy concentration. The oxidation state of as-synthesized R-MoO_{3-x} was confirmed by TGA and XPS. TGA was performed in either air or argon atmosphere using a TA SDT Q600 analyser at a heating rate of 10 °C min^{-1}. XPS analysis was performed using a Kratos Axis Ultra DLD with a monochromatic Al (Kα) radiation source. The charge neutralizer filament was used to control charging of the sample, 20 eV pass energy was used with a 0.05 eV step size, and scans were calibrated using the C 1*s* peak shifted to 284.8 eV. The samples were etched with an argon beam (raster size 5 mm × 5 mm) for 30 s. The integrated area of the peaks was found using the Casa-XPS software, and atomic ratios were also found using this software. The atomic sensitivity factors used were from the Kratos library within the Casa software.

Structural characterization. The phase of each MoO_3 sample was identified by XRD (Rigaku Miniflex II) using Cu–Kα ($\lambda = 1.54$ Å) radiation. The Brunauer–Emmett–Teller surface area was calculated from the nitrogen adsorption isotherms, which were collected on a Micromeritics ASAP 2010 gas adsorption analyser. The particle size and shape of MoO_3 samples were characterized by TEM (T12, FEI) and SEM (Nova NanoSEM 230, FEI). Atomic force microscopy imaging was performed on a Bruker Dimension Icon system under tapping mode.

Powder XRD for lattice parameter determination. Powder XRD was performed to compare the (020), (040) and (060) peaks position in each MoO_3 in a PANalytical X'Pert Pro operating with Cu Kα ($\lambda = 1.54$ Å) using a 0.008° step size, a voltage of 45 kV, and a current of 40 mA. Samples were prepared from a mixture of MoO_3 and 9.1% (w/w) silicon. After the composite was mixed in an agate mortar, a thin layer was packed onto a quartz slide for measurement. The silicon (111) reflection at 28.44° and the (220) reflection at 47.29° were used as reference peaks.

Electrochemical characterization. Electrochemical measurements were made using a three-electrode cell in which MoO_3 thin-film electrodes served as working electrodes. To prepare these electrodes, each MoO_3 sample (=40 μg) was suspended in ethanol and drop-cast on an O_2-plasma-treated stainless-steel current collector (1 cm^2 area). The weight of active material was measured by a microbalance (Cahn C-31, 0.1 μg resolution). One molar $LiClO_4$ in propylene carbonate was used as electrolyte and lithium metal foils were used as reference and counter electrodes. Cyclic voltammetry was performed between 1.5 and 3.5 V versus Li^+/Li using a PAR EG&G 273A Potentiostat. In Fig. 3 and Fig. 5, the samples were pre-cycled at 10 mV s^{-1} for 10 cycles (Fig. 3) and 5 cycles (Fig. 5) to stabilize their response before the measurements. All electrochemical measurements were performed in an argon-filled glovebox.

***Ex situ* XPS.** For the *ex situ* XPS (Kratos Axis Ultra DLD) experiment, R-MoO_{3-x} and F-MoO_3 working electrodes were lithiated and delithiated by using cyclic voltammetry. After 5 cycles at 10 mV s^{-1}, the sample was cycled at 5 mV s^{-1} to the specific potential. The cycled working electrodes were removed from the cell, washed with dimethyl carbonate and dried overnight in the argon-filled glovebox. These electrodes were loaded on the XPS sample holder in the glovebox and sealed in the XPS transfer chamber.

***Ex situ* XRD.** *Ex situ* XRD was performed in a Bruker Discover D8 operating with Cu Kα ($\lambda = 1.54$ Å) using a 0.035° step size, a voltage of 40 kV, and a current of 40 mA. The samples were prepared by galvanostatically discharging and charging R-MoO_{3-x} and F-MoO_3 at a C/5 rate. Those cycled electrodes were washed in dimethyl carbonate and dried for 24 h, and then sealed in 64 μm polyimide tape to prevent exposure to the environment. All preparation steps for the *ex situ* samples were performed in an argon-filled glovebox with O_2 below 1 ppm. Peak positions were calibrated using the stainless-steel current collector.

Electronic conductivity measurement. For the bulk electrical conductivity measurement, each MoO_3 sample was deposited on ITO-coated glass, which had been partially etched (10-μm-thick). Contacts were placed on the top and under the bottom of the samples and the latter (bottom contact) was made on the ITO connected to the bottom of the film. We measured electrical resistivity using a Solartron 1287 potentiostat.

DFT calculations. DFT calculations were used to study crystal structures, electronic properties and lithium intercalation voltages of R-MoO_{3-x}. We used the Perdew–Burke–Ernzerhof[42] exchange–correlation functional and the projector augmented wave method[43] as implemented in the Vienna Ab Initio Simulation Package[44] in all our calculations. To describe both the polaron and the vdW gap in R-MoO_{3-x}, we adopted the DFT+U method[45] for on-site Coulomb interaction and the optB88-vdW functional[46] for nonlocal correlation effects. The formalism of ref. 45 was employed to express the on-site Coulomb interaction with $U_{\mathrm{eff}} = 6$ eV for Mo ions. The DFT+U predictions for the polaron energies and migration barriers in MoO_3 were found previously to agree well with the results of calculations employing a screened hybrid exchange functional[47]. Generally, the DFT+U approach is expected to be applicable when the polaron is localized in the transition metal *d* orbitals, as is the case with Mo^{4+} and Mo^{5+} (ref. 48), but may fail in systems where the polaron has significant weight on the O *p* orbitals, such as TiO_2 (ref. 49). A plane wave basis set with an energy cutoff of 500 eV was used to expand the electronic wavefunctions. The Brillouin zone was sampled on a 2 × 2 × 2 Monkhorst–Pack[50] k-point mesh. Atomic coordinates were fully relaxed until all of the forces were below 0.02 eV $Å^{-1}$.

We used bulk supercells of MoO_3 containing 36 formula units. Calculations for reduced MoO_{3-x} were performed with one O vacancy in the supercell, corresponding to $x = 0.028$. We considered all symmetrically inequivalent O vacancy sites and studied representative polaron configurations that differ by the distances between the vacancy and the polarons. The composition of reduced MoO_3 in DFT calculations is lower than that in our reduced samples, which results in slightly smaller interlayer separation distances. However, the deviation between the *b* lattice parameter used in the DFT calculations and the measured value for the fully reduced sample is only 0.13 Å, or less than 1%. This difference is small and will not affect the calculated intercalation energies significantly. Furthermore, the effects of different exchange–correlation functionals on the predicted van der Waals gap for stoichiometric MoO_3 were studied previously, and it was found that optB88-vdW produces good agreement with experimental data[51].

The formation enthalpy of oxygen vacancy in R-MoO_{3-x} is defined by the following expression:

$$H_{\mathrm{f}} = H\left[\left(\mathrm{MoO}_{3-x/n}\right)_n\right] + \frac{x}{2}H^{\circ}\left[\mathrm{O}_2(g)\right] - H\left[(\mathrm{MoO}_3)_n\right]$$

where $H[(MoO_{3-x/n})_n]$ is the enthalpy of a bulk supercell of R-MoO_{3-x} with oxygen vacancies, $H[(MoO_3)_n]$ is the enthalpy of bulk MoO_3, and $H[O_2]$ is the enthalpy of an oxygen molecule in the triplet state. The enthalpies of bulk phases ($(MoO_{3-x/n})_n$, $(MoO_3)_n$) can be accurately approximated by the DFT total energies, while enthalpy value of gas phase (O_2) cannot be accurately calculated from DFT. Thus, we approximated $H^{\circ}[O_2(g)]$ by using the reaction enthalpy of the following reaction under standard conditions: $MoO_2(cr) + \frac{1}{2}O_2(g) \rightarrow MoO_3(cr)$ (ref. 52), and the DFT total energies of MoO_2 and MoO_3:

$$\frac{1}{2}H^{\circ}\left[\mathrm{O}_2(g)\right] \approx E\left[\mathrm{MoO}_3\right] - E\left[\mathrm{MoO}_2\right] - \Delta H_r^{\circ}$$

The calculated dissociation energy of an oxygen molecule is 5.6 eV, which is in reasonable agreement with the experimental value of 5.2 eV. We point out that the dissociation energy of an oxygen molecule calculated from DFT directly is 6.8 eV, which overestimates the experimental value by 1.6 eV.

Using lithium metal as a reference electrode, the voltage of lithium insertion in the dilute limit is calculated from[53]

$$\mathrm{V} = \frac{\Delta G}{e}$$

where ΔG is the free energy of lithium intercalation in the dilute limit in bulk pure MoO_3 or R-MoO_{3-x}. ΔG can be calculated from the following expression:

$$\Delta\mathrm{G} = \mathrm{G}\left[(\mathrm{MoO}_3)_n\,\mathrm{Li}\right] - n\mathrm{G}\left[\mathrm{MoO}_3\right] - \mathrm{G}[\mathrm{Li}]$$

where $G[(MoO_3)_nLi]$ is the total free energy of a bulk supercell of pure MoO_3 or R-MoO_{3-x} with a lithium atom, $G[MoO_3]$ is the total free energy of pure or reduced bulk MoO_3, and G[Li] is the total free energy of Li metal in the body-centered cubic phase.

References

42. Perdew, J. P., Burke, K. & Ernzerhof, M. Generalized gradient approximation made simple. *Phys. Rev. Lett.* **77,** 3865–3868 (1996).
43. Dal Corso, A. Projector augmented wave method with spin–orbit coupling: applications to simple solids and zincblende-type semiconductors. *Phys. Rev. B* **86,** 08135 (2012).
44. Kresse, G. & Furthmuller, J. Efficiency of *ab-initio* total energy calculations for metals and semiconductors using a plane-wave basis set. *Comput. Mater. Sci.* **6,** 15–50 (1996).

45. Dudarev, S. L. *et al*. Electron-energy-loss spectra and the structural stability of nickel oxide: An LSDA+U study. *Phys. Rev. B* **57,** 1505–1509 (1998).
46. Klimes, J., Bowler, D. R. & Michaelides, A. Van der Waals density functionals applied to solids. *Phys. Rev. B* **83,** 195131 (2011).
47. Ding, H. *et al*. Computational investigation of electron small polarons in α-MoO_3. *J. Phys. Chem. C* **118,** 15565–15572 (2014).
48. Ong, S. P., Chevrier, V. L. & Ceder, G. Comparison of small polaron migration and phase separation in olivine $LiMnPO_4$ and $LiFePO_4$ using hybrid density functional theory. *Phys. Rev. B* **83,** 075112 (2011).
49. Cheng, J., Sulpizi, M., VandeVondele, J. & Sprik, M. Hole localization and thermochemistry of oxidative dehydrogenation of aqueous rutile TiO_2(110). *ChemCatChem* **4,** 636–640 (2012).
50. Monkhorst, H. J. & Pack, J. D. Special points for Brillouin-zone integrations. *Phys. Rev. B* **13,** 5188–5192 (1976).
51. Ding, H., Ray, K. G., Ozolins, V. & Asta, M. Structural and vibrational properties of α-MoO_3 from van der Waals corrected density functional theory calculations. *Phys. Rev. B* **85,** 012104 (2012).
52. Staskiewicz, B. A., Tucker, J. R. & Snyder, P. E. The heat of formation of molybdenum dioxide and molybdenum trioxide. *J. Am. Chem. Soc.* **77,** 2987–2989 (1955).
53. Aydinol, M. K., Kohan, A. F. & Ceder, G. *Ab initio* calculation of the intercalation voltage of lithium transition metal oxide electrodes for rechargeable batteries. *J. Power Sources* **68,** 664–668 (1997).